minerals

MDPI

Article

Geochemistry, Zircon U–Pb Ages, and Hf Isotopes of the Devonian Mafic and Acidic Dykes of the Jinba Gold Deposit, NW China: Petrogenesis and Tectonic Implications

Fang Xia, Shunda Li *, Lingling Gao and Chuan Chen

Xinjiang Key Laboratory for Geodynamic Processes and Metallogenic Prognosis of the Central Asian Orogenic Belt, College of Geology and Mining Engineering, Xinjiang University, Urumqi 830047, China; cumtmaple@163.com (F.X.); gllgaoling@xju.edu.cn (L.G.); xjzycc2017@163.com (C.C.)

* Correspondence: shunda@xju.edu.cn; Tel.: +86-18844593361

Abstract: The Jinba deposit is an orogenic gold deposit located in the Markakuli shear zone, in the southern part of the Altay orogenic belt, northwestern China. Several granite and diorite dykes are present in the area of the mine, with ore bodies occurring in the diorite dykes. However, the diagenetic age, genesis, and evolution of these magmas, and the tectonic setting of the dyke emplacement process, remain unclear. The present study is based on a detailed geological survey, zircon U–Pb dating, Lu–Hf isotopes, and geochemical analysis of the granitic and diorite dykes. The crystallization ages of the granitic and diorite dykes are 384.5 ± 1.2 Ma and 393.9 ± 3.5 Ma, respectively, which indicates formation in the Early to Middle Devonian. Zircon $\varepsilon_{Hf(t)}$ values of the granitic and diorite dykes are 1.43 to 5.2 and −4.47 to −1.18, respectively, with a corresponding two-stage model of depleted mantle (T_{DM2}) ages of 1046 to 1285 Ma and 1242 to 2623 Ma, respectively. This indicates that the granitic and diorite dykes were formed by the mixing of mantle magma and crustal materials to varying degrees, and diorite dykes are more obviously contaminated by the lower crust. Geochemical analysis shows that the granite dykes have a high SiO_2 (72.51%–74.87%) and moderate Al_2O_3 (12.88%–14.04%) content, a total alkali of ($K_2O + Na_2O$ = 5.51%–6.44%), and aluminous (A/CNK = 1.0–1.02). Granite dykes are enriched in LREE and Th, U, and Pb, and depleted in P, Sr, and Nb elements, with clear Eu negative anomalies (δEu = 0.62~0.66). The SiO_2 content of diorite dykes is 51.48%–53.71%, Al_2O_3 contents are high (14.70%–15.99%), K_2O is 1.94%–2.54%, Na_2O is 2.97%–3.96%, MgO contents are high (5.15%–6.46%), and TFe_2O_3 is (13.42%–15.13%), enriched Sr, U, Pb, deficient Th elements, rare earth fractionation is not obvious, and Eu anomaly is not obvious (δEu = 0.93~1.1). We conclude that the Early to Middle Devonian magmatism in the southern margin of Altay (which corresponds to the Jinba gold deposit) may have formed in an island arc-related subduction environment.

Keywords: Altay orogenic belt; geochemistry; zircon U–Pb; Hf isotopes; Jinba gold deposit

check for updates

Citation: Xia, F.; Li, S.; Gao, L.; Chen, C. Geochemistry, Zircon U–Pb Ages, and Hf Isotopes of the Devonian Mafic and Acidic Dykes of the Jinba Gold Deposit, NW China: Petrogenesis and Tectonic Implications. *Minerals* **2022**, *12*, 871. https://doi.org/10.3390/min12070871

Academic Editor: Léo Afraneo Hartmann

Received: 1 June 2022
Accepted: 6 July 2022
Published: 9 July 2022

1. Introduction

The Altay orogenic belt is located at the junction of China, Mongolia, Russia, and Kazakhstan, and is an important part of the Central Asian Orogenic Belt (CAOB) [1–6]. The CAOB experienced Paleozoic accretion and Meso-Cenozoic intracontinental orogenesis [7–10]. It is characterized by complex tectonic and orogenic activity, frequent magmatic activity, and an extensive distribution of intrusive rocks, volcanic rocks, and subvolcanic rocks. This makes the CAOB, and specifically the Altay area, ideal for the study of tectonic evolution, crustal accretion, and mineralization–tectonics relationships. Indeed, there has been a great deal of research on the intrusive, volcanic, and subvolcanic rocks in the area; however, there are differing opinions on the formation age, source, and evolution of the magmatic materials, tectonic environment, and its relation to mineralization [11–17].

The Jinba gold deposit is located in the back arc basin of the Kelan in the southern margin of the Altay orogenic belt. Studies on the deposit mainly focus on its geological characteristics, genesis, metallogenic chronology, and exploration potential [18–22]. However, there is little research on the magmatic rocks of the Jinba deposit, especially on granitic and diorite dykes. It is worth noting that some ore bodies of the Jinba gold deposit occur within diorite dykes. In addition, the relationship between the magmatic activity of these dykes and the mineralization at Jinba is not clear at present. The granitic and diorite dykes are specifically located in the Habahe pluton, which is the largest intrusive body in the area.

The Habahe pluton is located on the northeastern side of the Markakuli fault, with an irregular-shaped outcrop area of approximately 180 km^2 [23]. It is a complex massif formed all at once and is mainly composed of medium and coarse-grained tonalite. The study of these dykes plays an important role in the geochronology, mantle origin, and tectonic evolution of the southern Altay, and provides important information on the relationship between the dykes and the coeval intrusive rocks in the area. The age, genesis, and tectonic setting of these dykes is clarified by the comprehensive study of whole-rock geochemical composition, zircon U–Pb chronology, and zircon Lu–Hf isotope data provided in the present study. Based on the results of this study and the available data for magmatic rocks in the southern Altay margin, their Devonian tectonic setting is discussed in order to provide insight into the relationship between dykes and mineralization and the tectonic evolution of the southern margin of the Altay orogenic belt.

2. Regional Geology

The Jinba deposit is located near the border between China and Kazakhstan and is the extension of the metallogenic belt in the Kazakhstan mining area. Exposed strata mainly include littoral and neritic sedimentary rocks of the Middle and Lower Devonian Tuokesalei formation. Volcano-sedimentary rocks are intercalated with carbonate rocks in the Middle Devonian Ashele formation. The intermediate-acid volcanic rocks of the Upper Devonian Qiye formation are in angular unconformity with the overlying and underlying strata [24]. Quaternary sediments are also present in the area. Fracture development is widespread in the area, with structures present in the northern and western parts of the area, and near north-to-south structures. The region's largest tectonic structure is the Irtysh fault zone, which divides the Siberian plate and the Kazakhstan–Junggar plate, as shown in Figure 1B [25]. The secondary fault system of the Irtysh fault zone, the Markakuli shear zone, affects the spatial distribution of intrusive rocks and ore deposits [26]. Magma activity is frequent in the area, and plutonic intrusive rocks and volcanic rocks are developed. Ultrabasic, basic, and acidic plutonic rocks are exposed, mainly middle to late Variscan intermediate-acidic and acidic units, which are mainly distributed along both sides of the Markakuli fault in the form of bedrock and rock strata and intruding into the strata of the Tuokesalei and Ashele formations. Basic to acidic outcrops occur in the form of rock strata, and the rock mass is relatively complex and small in area. There are also acidic, intermediate, and basic dykes and wall rocks distributed along the direction of the regional fault zone. The volcanic rocks crop out to the northeast of the Markakuli fault, with a NWN-SE distribution. They are mainly intermediate-acidic and intermediate units, with few basic rocks [27]. The Ashele copper-zinc deposit, Zhelande, Saidu, Tuokuzibayi, and Jinba gold deposits have been discovered in the area. (Figure 1A).

At present, six ore bodies have been proved in the Jinba deposit [21] (Figure 2A). Mineralization types can be divided into altered-rock type and quartz-vein type. Altered-rock-type orebodies mainly occur in altered diorite dykes, which are vein-like or lenticular, including orebodies I, II, III, and V (Figure 2B).

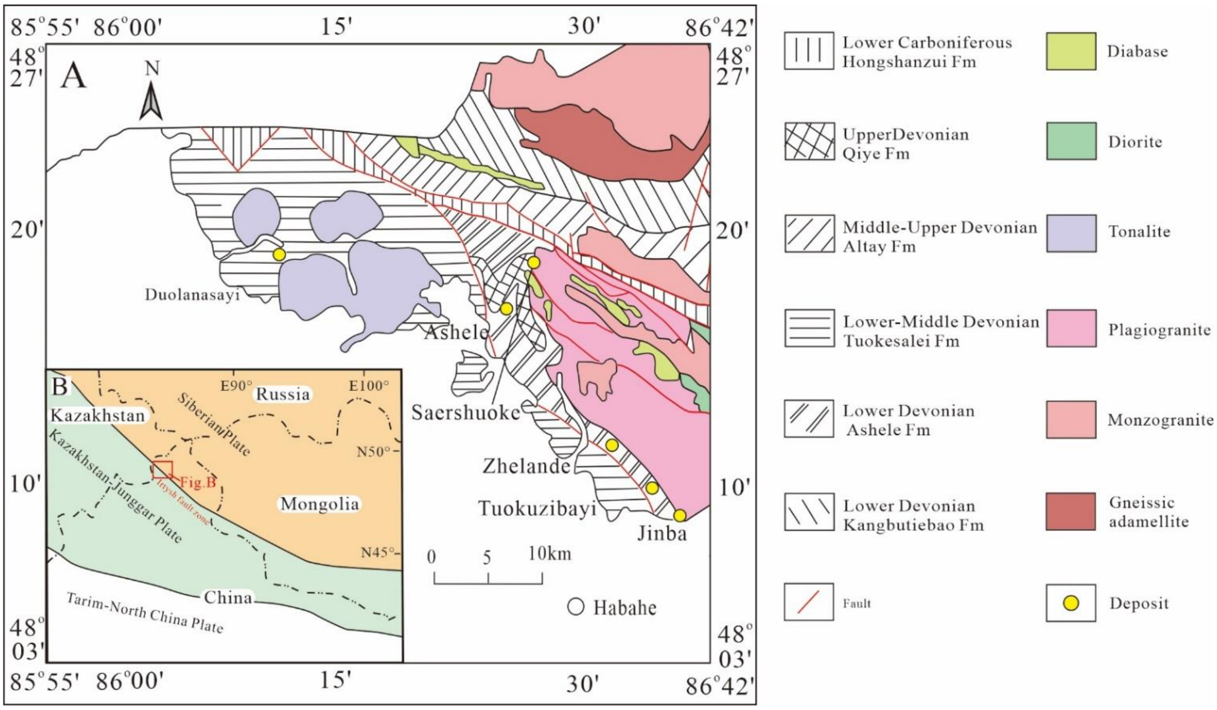

Figure 1. (**A**) Tectonic map of western China. (**B**) Regional geological map of the southwestern Chinese AOB (modified after Zhan et al. [20]).

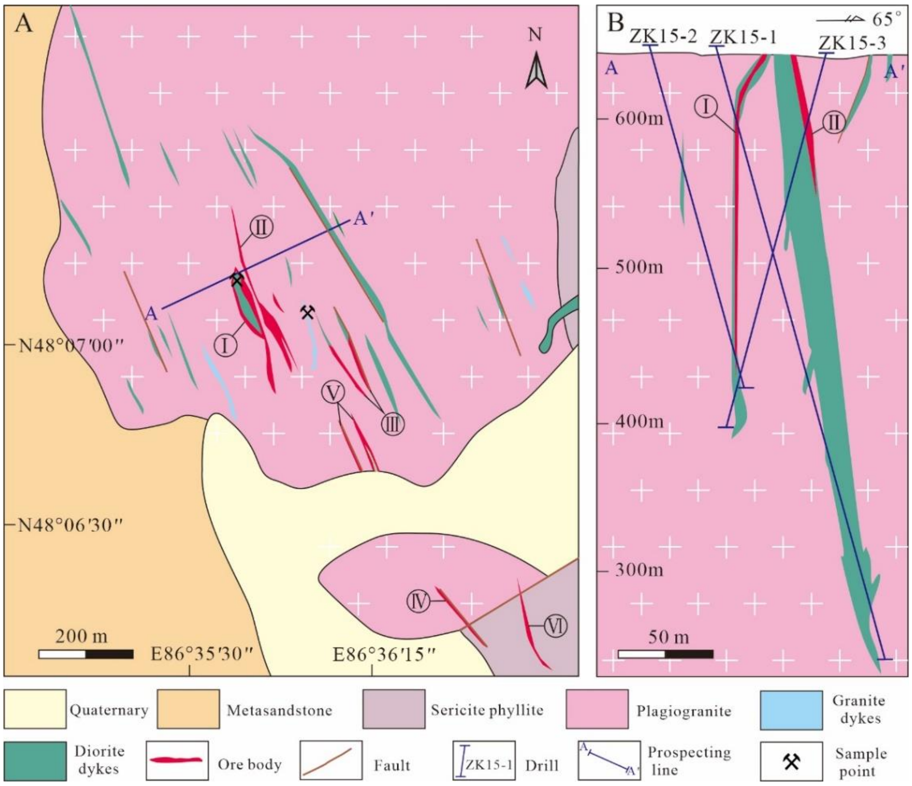

Figure 2. (**A**) Geological map of the Jinba gold deposit (I–VI indicates the number of ore body, modified after Wang et al. [21]). (**B**) Geological cross–section of the orebodies (modified after Wang et al. [21]).

3. Analytical Methods

3.1. Sample Descriptions

The granite dyke intrudes into the Habahe pluton, Habahe County, northwest China. Their hand specimens are predominantly grayish white, with rough granite structures and massive structures (Figure 3A). The main mineral composition is feldspar (60%), quartz (30%), biotite (10%), and a small amount of hornblende. Quartz contains a small amount of basic mineral inclusions, mainly biotite and hornblende (Figure 3B). The main accessory minerals are zircon, apatite, and magnetite.

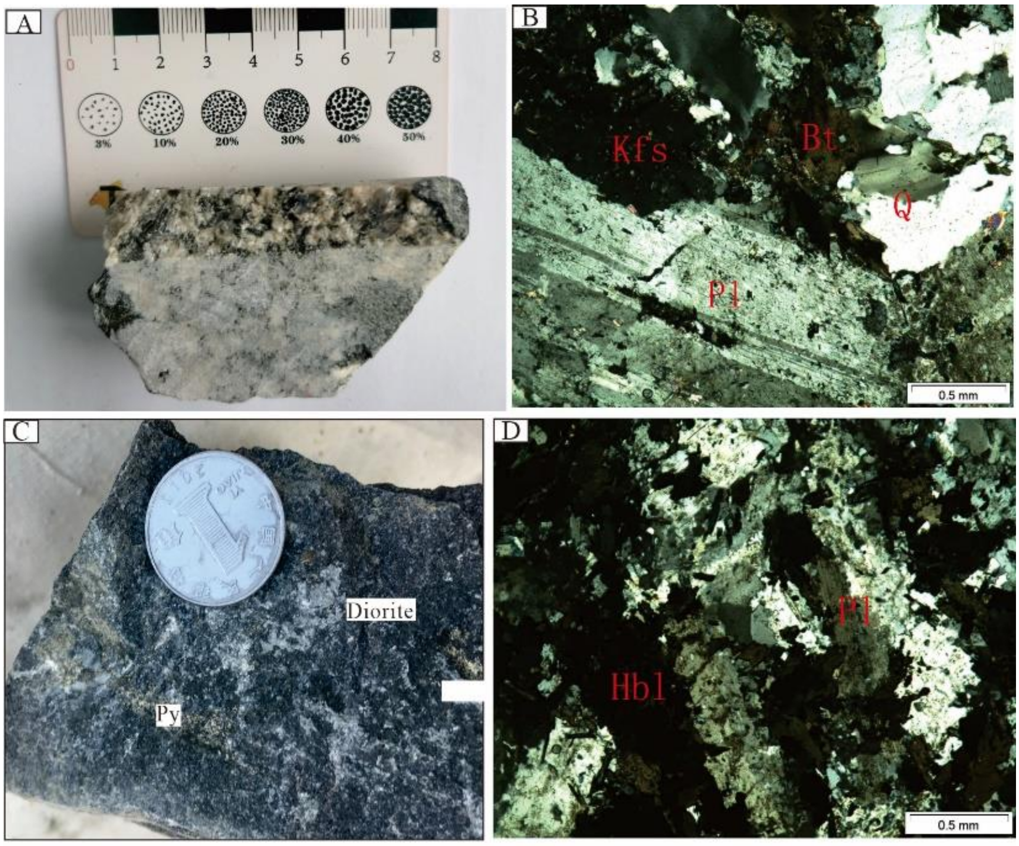

Figure 3. Hand specimen and photomicrographs of rocks from Jinba gold deposit. (**A**)—Granite dyke hand specimen, (**B**)—Photomicrograph of the granite dyke, (**C**)—Diorite dyke hand specimen, (**D**)—Photomicrograph of the diorite dyke. Q—quartz; Pl—plagioclase; Kfs—K-feldspar; Hbl—hornblende; Bt—biotite.

Diorite dykes are gray in color, with variable complementary semi-idiomorphic granular structure and massive structure (Figure 3C). Plagioclase: 60%, euhedral, semi-euhedral plate, poly-flake double crystal, sodium compound double crystal development, plate length 0.2–1.2 mm, scattered distribution. Hornblende: 35%, columnar, granular, less with hexagonal geometric section, hornblende cleavage development, particle size 0.15–1.2 mm, scattered distribution. Quartz: small amount, xenomorphic granular, particle size 0.1–0.5 mm, star-dot distribution. Apatite: small amount, columnar, granular. Opaque minerals: 2%–3%, xenomorphic granular and irregular granular (Figure 3D). More distributed in hornblende edge.

3.2. LA-ICP-MS Zircon U–Pb Geochronology

Zircon grains were separated from the diorite and granite samples by conventional magnetic and density techniques. Zircon grains free of visible inclusions and fractures were handpicked, embedded in epoxy resin, and polished to expose grain centers. The polished grains were further examined by cathodoluminescence (CL) imaging using a JXA-8100 electron microprobe at the Langfang Regional Geological Survey, Langfang, China. Zircon U–Pb dating and trace element analyses were performed at the Beijing Yandu Zhongshi Testing Technology Co. LTD (Beijing, China) using a Brooke M90 ICP-MS. The detailed method has been described by Liu et al., [28]. Data acquisition time was ~20–30 s for blank signal and ~50 s for sample signal. Data processing was carried out with ICPMS Data Cal software [28]. U–Pb isotope fractionation effects were calibrated using zircon 91500 as the external standard [29], and NIST 610 glass was used for instrument optimization. Analytical data are presented on U–Pb concordia diagrams with 2σ errors, and weighted mean ages are quoted at the 95% confidence level using ISOPLOT software [30].

3.3. Major and Trace Element Analyses

The major and trace element contents of 5 diorite samples and 5 granite samples were obtained at ALS Mineral-ALS Chemex in Guangzhou, China. The samples were first crushed with a steel-jaw crusher and then ground to 200 mesh with an agate mortar. Major elements were analyzed by X-ray fluorescence ME-XRF26X, and trace element concentrations were determined by rare earth mass spectrometry (ME-MS81) and inductively coupled plasma atomic emission spectrometry. A mixture of HF and HNO_3 was added to the melted sample and tartaric acid digestion was performed according to the analytical method of [31] (Method ME-MS61). The samples were stored at 190 °C for 48 h with indium as internal standard and the China National Standard sample as monitoring sample. The analysis accuracy of major and trace elements (REE) is better than 5% and 10%, respectively. Ignition losses (LOI) for all samples were obtained by heating them in a pre-fired silicon crucible at 1000 °C for 1 h and recording the percentage of weight loss.

3.4. In Situ Zircon Lu–Hf Isotope Analysis

Zircon Lu–Hf isotope analysis of previous U–Pb sites was performed using a Neptune Plus MC-ICP-MS and a New Wave UP 213 laser ablation detector. The work was conducted at the Beijing Yandu Zhongshi Testing Technology Co., LTD. Beam diameter was 45 μm and laser repetition rate was 10 Hz. Helium and argon were, respectively, used as carrier gas and supplementary gas for analysis. The international zircon standard GJ1 was adopted as the external standard. Operating conditions were provided by [32,33]. Using 91500, MON, and GJ-1 as reference standards, the recommended $^{176}Hf/^{177}Hf$ ratios are 0.282307, 0.282739, and 0.282015, respectively. It is assumed that the average crustal $^{176}Lu/^{177}Hf$ ratio is 0.015, and the current chondritic $^{176}Hf/^{177}Hf$ and $^{176}Lu/^{177}Hf$ ratios are 0.282772 and 0.0332, respectively. $^{176}Lu/^{177}Hf$ ratios in the mean mantle are 0.28325 and 0.0384 [34,35]. The decay constant of ^{176}Lu is 1.865×10^{-11} year^{-1} [36].

4. Results

4.1. Zircon U–Pb Ages

Zircon LA-ICP-MS, U–Pb dating, and trace element analysis results are shown in Table 1. Most of the zircon specimens in the samples studied show similar signatures. Zircon grains in the samples are irregular in shape (Figure 4). Grain sizes range from 50 to 200 μm with aspect ratios of 1:1 to 2:1. CL imaging reveals that most grains have fine oscillatory growth zones, which suggest a magmatic origin [37].

Table 1. LA-MC-ICP-MS U–Pb data of zircons from granite and diorite dykes of the Jinba gold deposit.

Sample	^{238}U	^{232}Th	Th	^{207}Pb/^{206}Pb		^{207}Pb/^{235}U		^{206}Pb/^{238}U		^{207}Pb/^{206}Pb		^{207}Pb/^{235}U		^{206}Pb/^{238}U	
	$\times 10^{-6}$	$\times 10^{-6}$	/U	Ratio	1σ	Ratio	1σ	Ratio	1σ	Age (Ma)	1σ	Age (Ma)	1σ	Age (Ma)	1σ
JB1-04	333	162	0.49	0.0550	0.0015	0.4599	0.0119	0.0606	0.0006	412.4	62	384.2	8	379.6	4
JB1-24	499	302	0.61	0.0543	0.0010	0.4545	0.0088	0.0607	0.0006	384.4	43	380.4	6	379.6	4
JB1-01	496	477	0.96	0.0549	0.0007	0.4613	0.0074	0.0609	0.0006	407.9	30	385.1	5	381.0	3
JB1-07	449	288	0.64	0.0559	0.0014	0.4683	0.0118	0.0609	0.0008	446.9	55	390.0	8	386.5	5
JB1-16	305	197	0.65	0.0547	0.0013	0.4602	0.0110	0.0610	0.0007	400.7	52	384.4	7	381.6	4
JB1-05	353	173	0.49	0.0553	0.0010	0.4648	0.0084	0.0610	0.0004	422.4	38	387.6	5	381.9	3
JB1-18	431	241	0.56	0.0546	0.0010	0.4603	0.0079	0.0611	0.0005	397.7	39	384.5	5	382.1	3
JB1-17	404	269	0.67	0.0529	0.0009	0.4473	0.0080	0.0612	0.0005	325.7	39	375.4	5	383.2	3
JB1-11	368	196	0.53	0.0535	0.0009	0.4522	0.0079	0.0613	0.0005	349.9	39	378.8	6	383.5	3
JB1-14	396	199	0.50	0.0554	0.0009	0.4675	0.0077	0.0613	0.0005	426.6	36	389.5	5	383.6	3
JB1-09	415	194	0.47	0.0548	0.0008	0.4640	0.0069	0.0614	0.0005	404.2	31	387.0	5	384.2	3
JB1-06	462	271	0.59	0.0560	0.0007	0.4732	0.0065	0.0615	0.0005	450.5	28	393.4	5	384.7	3
JB1-10	384	186	0.49	0.0545	0.0007	0.4608	0.0062	0.0615	0.0005	389.9	28	384.8	4	384.8	3
JB1-03	424	236	0.56	0.0555	0.0007	0.4693	0.0063	0.0615	0.0005	430.8	29	390.7	4	384.8	3
JB1-19	564	372	0.66	0.0543	0.0009	0.4616	0.0082	0.0615	0.0005	384.2	36	385.3	6	384.9	3
JB1-08	515	293	0.57	0.0550	0.0009	0.4658	0.0069	0.0616	0.0005	410.9	35	388.3	5	385.1	3
JB1-29	745	509	0.68	0.0550	0.0009	0.4673	0.0075	0.0616	0.0006	414.2	35	389.3	5	385.1	3
JB1-02	433	280	0.65	0.0542	0.0009	0.4599	0.0078	0.0616	0.0005	380.4	39	384.2	5	385.1	3
JB1-23	442	230	0.52	0.0540	0.0010	0.4586	0.0075	0.0616	0.0005	370.6	41	383.3	5	385.3	3
JB1-13	440	256	0.58	0.0544	0.0007	0.4619	0.0074	0.0616	0.0007	388.3	30	385.6	5	385.4	4
JB1-22	513	271	0.53	0.0546	0.0008	0.4640	0.0066	0.0617	0.0006	397.8	31	387.0	5	385.9	3
JB1-28	550	314	0.57	0.0538	0.0009	0.4582	0.0069	0.0618	0.0006	361.8	37	383.0	5	386.4	4
JB1-27	586	355	0.61	0.0544	0.0007	0.4642	0.0059	0.0618	0.0005	387.1	27	387.1	4	386.5	5
JB1-21	524	318	0.61	0.0542	0.0006	0.4625	0.0058	0.0618	0.0005	381.2	25	386.0	4	386.5	3
JB1-15	417	188	0.45	0.0543	0.0007	0.4621	0.0065	0.0618	0.0005	381.6	31	385.7	5	386.6	3
JB1-26	445	215	0.48	0.0553	0.0010	0.4709	0.0079	0.0618	0.0006	425.5	39	391.8	5	386.7	4
JB1-20	976	789	0.81	0.0547	0.0006	0.4661	0.0047	0.0618	0.0005	401.8	24	388.5	3	386.8	3
JB1-12	470	245	0.52	0.0537	0.0006	0.4588	0.0058	0.0619	0.0005	359.4	27	383.4	4	387.4	3
JB1-25	464	188	0.40	0.0539	0.0013	0.4610	0.0132	0.0620	0.0008	364.8	56	385.0	9	387.5	5
JB2-06	515	318	0.62	0.0559	0.0009	0.4902	0.0024	0.0628	0.0002	412.7	41	397.9	4	393.6	3
JB2-04	316	186	0.59	0.0554	0.0012	0.4852	0.0074	0.0625	0.0004	404.7	46	386.1	6	394.8	3
JB2-11	335	167	0.50	0.0544	0.0011	0.4765	0.0113	0.0631	0.0009	383.3	47	393.5	5	391.1	5
JB2-09	475	144	0.30	0.0548	0.0013	0.4713	0.0146	0.0629	0.0007	405.1	68	382.6	8	392.1	4
JB2-01	289	137	0.47	0.0570	0.0009	0.4914	0.0086	0.0626	0.0005	491.2	36	405.8	6	391.4	3
JB2-02	413	269	0.65	0.0552	0.0012	0.4772	0.0103	0.0627	0.0005	420.1	48	396.2	7	392.2	3
JB2-03	741	511	0.69	0.0555	0.0010	0.4823	0.0091	0.0630	0.0008	433.3	41	399.6	6	393.9	5
JB2-05	488	222	0.46	0.0542	0.0012	0.4702	0.0098	0.0632	0.0007	377.6	50	391.3	7	394.9	4
JB2-08	375	236	0.63	0.0547	0.0014	0.4781	0.0052	0.0627	0.0009	420.1	53	396.0	10	394.4	6
JB2-12	647	397	0.61	0.0569	0.0006	0.4883	0.0103	0.0628	0.0010	386.8	23	399.0	6	392.3	3
JB2-10	351	208	0.59	0.0553	0.0011	0.4799	0.0114	0.0632	0.0006	384.3	35	393.7	5	393.3	5
JB2-07	379	237	0.62	0.0548	0.0015	0.4751	0.0067	0.0628	0.0009	417.5	25	394.3	3	393.2	5

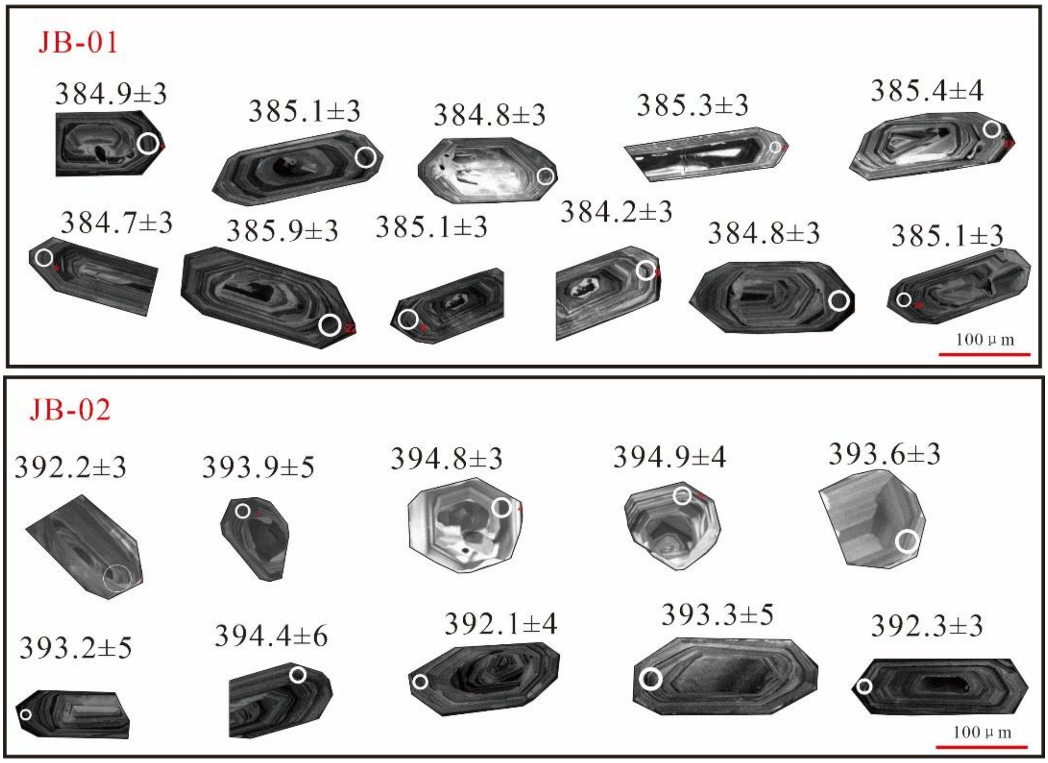

Figure 4. Typical cathodoluminescence images of typical zircon grains in the Jinba gold deposit. JB-01 is a granite dyke and JB-02 is a diorite dyke.

4.1.1. Granite Dykes

The ^{232}Th content of zircons found in granite ranges from 197,307 to 789,253 ppb, ^{238}U content ranges from 305,346 to 975,726 ppb, and Th/U ratios are between 0.40 and 0.96. Twenty-nine zircon grains fall in the range of 379.6–386.8 Ma with a weighted mean age of 384.5 ± 1.2 Ma (MSWD = 0.42, n = 29) (Figure 5A), which we interpret as the emplacement age of the granitic dykes.

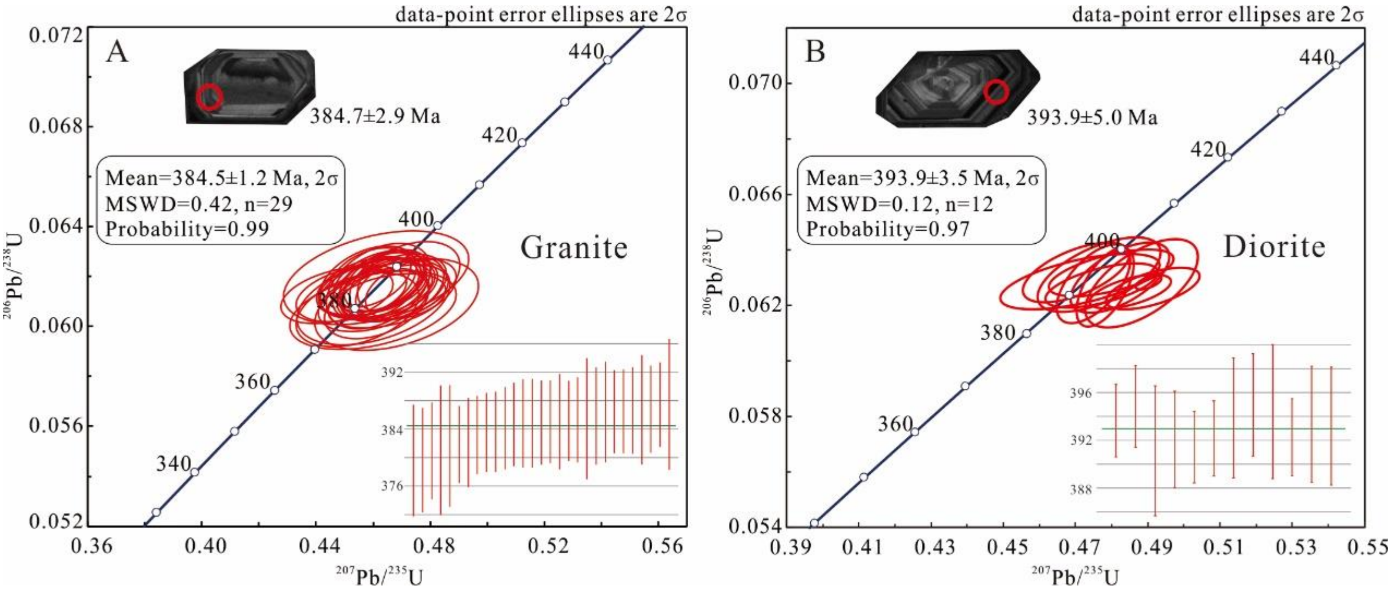

Figure 5. Zircon U–Pb age diagrams of granite and diorite from the Jinba gold deposit. (**A**) Zircon U–Pb age of granitic dykes; (**B**) Zircon U–Pb age of diorite dykes.

4.1.2. Diorite Dykes

The ^{232}Th content of zircons found in diorite ranges from 137,202 to 510,852 ppb, ^{238}U content ranges from 289,041 to 741,002 ppb, and Th/U ratios are between 0.30 and 0.69. Twelve zircon grains fall in the range of 394.9–391.1 Ma with a weighted mean age of 393.0 ± 2.2 Ma (MSWD = 0.10, n = 12) (Figure 5B), interpreted as the emplacement age of the diorite dykes.

4.2. Zircon Hf isotopic compositions

Zircon Hf isotopic analysis results are shown in Table 2 and Figure 6. The values of ^{176}Yb/^{177}Hf and ^{176}Lu/^{177}Hf range from 0.035134 to 0.076424, and 0.001353 to 0.002847, respectively. Zircon $\varepsilon_{Hf(t)}$ values of granite range from 1.43 to 5.2, with an average of 3.24. The corresponding T_{DM2} model ages range from 1046 to 1285 Ma, with an average of 1171 Ma. The values of ^{176}Yb/^{177}Hf and ^{176}Lu/^{177}Hf are 0.029446–0.112701 and 0.001033–0.004123, respectively. The zircon $\varepsilon_{Hf(t)}$ of diorite dykes is between −4.47 and −1.18, with an average of −2.59. Corresponding TDM2 model ages range from 1242 to 1668 Ma, with an average of 1464 Ma. Thus, it can be seen from the above data that the granitic dyke material originated from the depleted mantle and was mixed with partially molten crust, while the diorite dyke material was derived from the lower crust (Figure 6).

Table 2. Hf isotope data of zircon from granite and diorite dykes of the Jinba gold deposit.

Sample No	Age	$^{176}Yb/^{177}Hf$	2σ	$^{176}Lu/^{177}Hf$	2σ	$^{176}Hf/^{177}Hf$	2σ	$\varepsilon_{Hf(0)}$	$\varepsilon_{Hf(t)}$	T_{DM1}	T_{DM2}	$f_{Lu/Hf}$
JB-1-01	381	0.038611	0.000855	0.001452	0.000032	0.282642	0.000023	−4.60	3.42	874	1157	−0.96
JB-1-02	385.1	0.027714	0.000329	0.001070	0.000013	0.282621	0.000024	−5.33	2.87	895	1195	−0.97
JB-1-03	384.8	0.048592	0.000146	0.001783	0.000006	0.282650	0.000024	−4.30	3.71	870	1141	−0.95
JB-1-04	379.6	0.045428	0.001634	0.001614	0.000058	0.282646	0.000023	−4.46	3.48	873	1151	−0.95
JB-1-05	381.9	0.067268	0.001984	0.002409	0.000050	0.282640	0.000025	−4.65	3.14	900	1175	−0.93
JB-1-06	384.7	0.051168	0.000476	0.001908	0.000012	0.282693	0.000022	−2.78	5.20	811	1046	−0.94
JB-1-07	386.5	0.047940	0.000193	0.001745	0.000008	0.282638	0.000028	−4.75	3.31	887	1168	−0.95
JB-1-08	385.1	0.051441	0.000546	0.001808	0.000018	0.282650	0.000026	−4.33	3.69	872	1143	−0.95
JB-1-09	384.2	0.058729	0.000897	0.002124	0.000035	0.282635	0.000025	−4.86	3.05	901	1182	−0.94
JB-1-10	384.8	0.044939	0.001281	0.001688	0.000052	0.282659	0.000021	−3.99	4.05	855	1119	−0.95
JB-1-11	383.5	0.035134	0.000219	0.001368	0.000009	0.282618	0.000022	−5.45	2.65	906	1207	−0.96
JB-1-12	387.4	0.053721	0.000940	0.001962	0.000027	0.282632	0.000024	−4.94	3.08	900	1183	−0.94
JB-1-13	385.4	0.054529	0.000811	0.001947	0.000025	0.282652	0.000026	−4.26	3.73	872	1140	−0.94
JB-1-14	383.6	0.057263	0.000913	0.001987	0.000024	0.282687	0.000022	−3.02	4.91	823	1064	−0.94
JB-1-15	386.6	0.038809	0.000141	0.001353	0.000005	0.282642	0.000027	−4.58	3.58	871	1151	−0.96
JB-1-17	383.2	0.060300	0.001188	0.002222	0.000050	0.282611	0.000024	−5.70	2.16	938	1238	−0.93
JB-1-18	382.1	0.076424	0.000684	0.002847	0.000026	0.282628	0.000025	−5.09	2.60	929	1209	−0.91
JB-1-19	384.9	0.051151	0.000905	0.001949	0.000027	0.282587	0.000023	−6.54	1.43	965	1285	−0.94
JB-1-21	386.5	0.053689	0.000318	0.002056	0.000007	0.282613	0.000024	−5.63	2.35	931	1229	−0.94
JB-2-02	396.2	0.032874	0.000340	0.001228	0.000007	0.282407	0.000025	−12.90	−4.47	1201	1668	−0.96
JB-2-03	399.6	0.112701	0.001062	0.004123	0.000018	0.282499	0.000028	−9.65	−2.21	1161	1516	−0.88
JB-2-05	391.3	0.045189	0.001260	0.001745	0.000044	0.282603	0.000020	−5.99	−2.22	938	1242	−0.95
JB-2-06	397.9	0.055345	0.000982	0.001929	0.000040	0.282605	0.000029	−5.91	−3.51	939	1393	−0.94
JB-2-10	393.7	0.029446	0.000385	0.001136	0.000011	0.281869	0.000030	−31.93	−14.93	1949	2623	−0.97
JB-2-12	399.0	0.031049	0.000368	0.001033	0.000007	0.282431	0.000025	−12.04	−1.18	1161	1545	−0.97

$\varepsilon_{Hf(t)} = 10{,}000 \times \{[(^{176}Hf/^{177}Hf)_S - (^{176}Lu/^{177}Hf)_S \times (e^{\lambda t} - 1)]/[(^{176}Hf/^{177}Hf)_{CHUR,0} - (^{176}Lu/^{177}Hf)_{CHUR} \times (e^{\lambda t} - 1)] - 1\}$. $T_{DM} = 1/\lambda \times \ln\{1 + [(^{176}Hf/^{177}Hf)_S - (^{176}Hf/^{177}Hf)_{DM}]/[(^{176}Lu/^{177}Hf)_S - (^{176}Lu/^{177}Hf)_{DM}]\}$. $f_{Lu/Hf} = (^{176}Lu/^{177}Hf)_S/(^{176}Lu/^{177}Hf)_{CHUR} - 1$. where, $\lambda = 1.867 \times 10^{-11}$ $year^{-1}$ (Soderlund et al. [38]); $(^{176}Lu/^{177}Hf)_S$ and $(^{176}Hf/^{177}Hf)_S$ are the measured values of the samples; $(^{176}Lu/^{177}Hf)_{CHUR} = 0.0332$ and $(^{176}Hf/^{177}Hf)_{CHUR,0} = 0.282772$ (Blichert-Toft and Albarède, 1997); $(^{176}Lu/^{177}Hf)_{DM} = 0.0384$ and $(^{176}Hf/^{177}Hf)_{DM} = 0.28325$ (Griffin et al. [32]); $(^{176}Lu/^{177}Hf)_{mean\ crust} = 0.015$; $fs = f_{Lu/Hf}$; $f_{DM} = [(^{176}Lu/^{177}Hf)_{DM}/(^{176}Lu/^{177}Hf)_{CHUR}] - 1$; t = crystallization time of zircon.

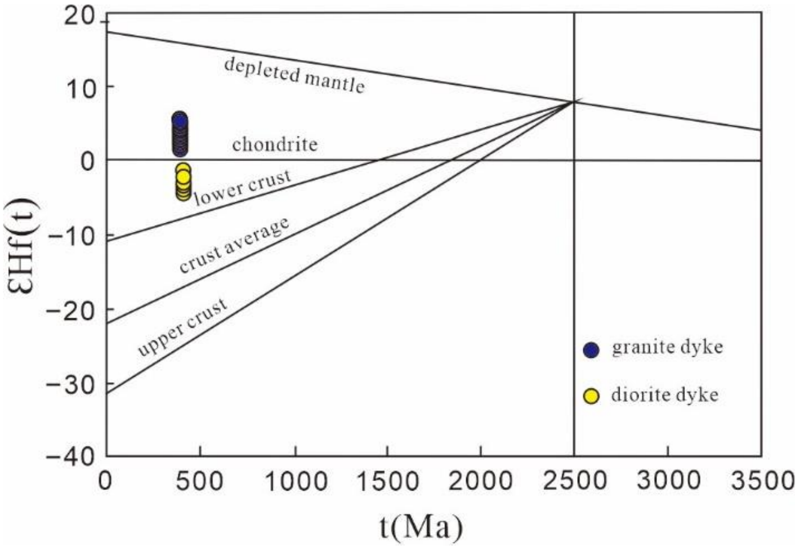

Figure 6. $\varepsilon_{Hf(t)}$—t plot of granite and diorite dykes from the Jinba gold deposit. (Base map after Guo et al. [39]).

4.3. Major and Trace Elements

4.3.1. Major Elements

Elemental analysis data of granite and diorite dykes are shown in Table 3. The results show that SiO_2 and Al_2O_3 contents of granite dykes are 72.51~74.87 wt%, and 12.88~14.04 wt%, respectively. Samples show A/CNK: 1.00~1.02, a Rittman index of 1.08~1.49, $K_2O + Na_2O$ of 5.51%~6.44%, P_2O_5 of 0.05%~0.06%, and CaO of 2.50%~2.89%.

Table 3. Major (%) and trace element (ppm) data from granite and diorite dykes of the Jinba gold deposit.

Sample No.	JB-1	JB-2	JB-3	JB-4	JB-5	JB-6	JB-7	JB-8	JB-9	JB-10
Rock Type **Age**	**Granite Dykes** **384 Ma**					**Diorite Dykes** **393 Ma**				
SiO_2%	74.87	73.32	73.51	72.82	72.51	53.71	51.61	51.48	53.05	52.18
TiO_2%	0.22	0.23	0.23	0.26	0.25	1.62	1.66	1.86	1.60	1.76
Al_2O_3%	12.88	13.02	13.36	14.04	13.08	15.03	14.70	15.99	14.96	14.84
TFe_2O_3%	2.75	2.76	3.09	3.08	3.09	14.04	15.13	13.42	14.82	14.55
MnO%	0.06	0.06	0.07	0.04	0.07	0.21	0.25	0.25	0.23	0.23
MgO%	0.65	0.65	0.77	0.63	0.69	5.61	5.60	6.46	5.15	5.88
CaO%	2.63	2.66	2.84	2.50	2.89	3.23	3.40	3.34	3.38	3.44
Na_2O%	3.14	3.24	3.44	4.46	3.11	3.26	3.15	3.96	2.97	3.62
K_2O%	2.66	2.53	2.12	1.98	2.40	2.54	2.10	1.96	1.94	1.98
P2O5%	0.05	0.05	0.05	0.06	0.05	0.21	0.16	0.19	0.17	0.18
LOI%	0.66	0.74	0.99	0.90	0.88	0.97	1.26	0.83	0.82	0.96
Total%	100.57	99.31	100.28	100.97	100.97	100.43	99.02	99.74	99.09	99.62
A/CNK	1.00	1.00	1.02	1.00	1.01	1.07	1.08	1.09	1.14	1.03
Mg#	31.9	31.8	33.0	28.8	30.7	44.2	42.3	48.8	40.78	44.5
V μg/g	32	36	38	43	41	329	418	306	390	335
Cr μg/g	10	20	20	30	20	10	20	10	10	20
Ni μg/g	2.3	2.2	2.3	3.0	2.6	4.9	6.7	6.1	4.8	5.0
Ga μg/g	11.5	11.9	12.0	11.6	12.2	16.8	19.7	17.8	20.7	19.3
Rb μg/g	86.0	90.7	71.1	75.6	92.1	87.2	81.7	64.9	50.0	67.2
Sr μg/g	130.5	102.5	160.5	188	113.5	155.5	128.5	168.5	162	159.4
Y μg/g	21.4	22.5	22.7	23.4	23.8	28.0	27.6	29.9	28.3	28.2
Zr μg/g	97	116	120	116	106	77	63	84	73	82
Nb μg/g	5.8	6.3	6.3	7.6	6.7	2.8	1.8	2.6	2.3	2.6
Cs μg/g	1.59	2.25	1.34	1.04	2.42	5.40	5.08	4.47	4.98	5.18
Ba μg/g	378	355	393	361.5	311	68.4	69.5	51.1	80.7	70.4
La μg/g	20.7	20.8	21.5	17.6	19.4	5.1	4.2	4.8	4.6	4.7
Ce μg/g	40.0	40.5	41.9	36.1	38.6	14.3	11.6	13.6	12.2	12.3
Pr μg/g	4.40	4.37	4.70	4.34	4.46	2.16	1.89	2.14	2.11	2.15
Nd μg/g	15.0	14.9	16.5	15.9	15.6	10.7	9.6	10.9	10.6	10.0
Sm μg/g	2.77	2.75	3.01	3.53	3.14	3.56	3.28	3.52	3.48	3.39
Eu μg/g	0.57	0.54	0.62	0.71	0.60	1.21	1.32	1.41	1.41	1.35
Gd μg/g	2.48	2.49	2.75	3.47	2.83	4.44	4.44	4.73	4.41	4.54
Tb μg/g	0.41	0.41	0.43	0.58	0.47	0.79	0.74	0.82	0.75	0.75
Dy μg/g	2.54	2.75	2.81	3.83	3.15	5.21	5.04	5.53	5.12	5.38
Ho μg/g	0.57	0.60	0.63	0.83	0.69	1.12	1.09	1.21	1.09	1.13
Er μg/g	1.72	1.91	1.88	2.68	2.14	3.21	3.17	3.44	3.21	3.24
Tm μg/g	0.29	0.33	0.31	0.44	0.36	0.50	0.47	0.52	0.50	0.49
Yb μg/g	2.03	2.24	2.22	2.26	2.56	3.17	3.07	3.41	3.30	3.38
Lu μg/g	0.34	0.37	0.37	0.53	0.43	0.48	0.45	0.49	0.48	0.44
Hf μg/g	2.8	3.2	3.3	3.4	3.1	2.1	1.9	2.3	2.0	2.0
Ta μg/g	0.50	0.54	0.47	0.58	0.57	0.15	0.11	0.16	0.13	0.14
Th μg/g	7.40	7.95	7.01	7.31	7.39	0.55	0.46	0.56	0.51	0.55
U μg/g	2.4	2.0	2.6	2.7	2.4	0.2	0.3	0.4	0.2	0.3
δEu	0.66	0.63	0.66	0.62	0.62	0.93	1.06	1.06	1.1	1.05
ΣLREE/ΣHREE	8.04	7.55	7.74	5.01	6.48	1.96	1.73	1.8	1.82	1.75
LaN/YbN	7.31	6.66	6.95	5.87	5.44	1.15	0.98	1.01	1.00	1.00

LOI = Loss on ignition. Mg# = Molecular Mg/(Mg + Fe). Fe_2O_3T are total iron. Normalizing values after Sun and McDonough (1989). Metaluminous and peraluminous fields, and diorite dykes fall within the hyperaluminous range.

The SiO_2 and Al_2O_3 contents of the diorite dykes are 51.48~53.71 wt% and 14.70~15.99 wt%, respectively. These dykes show weak peraluminite (A/CNK: Terman index in 1.03~1.14), 3.0~5.14, $K_2O + Na_2O$ (4.91%~5.92%), P_2O_5 (0.16%~0.21%), and CaO (3.23%~3.44%) (Figure 7a).

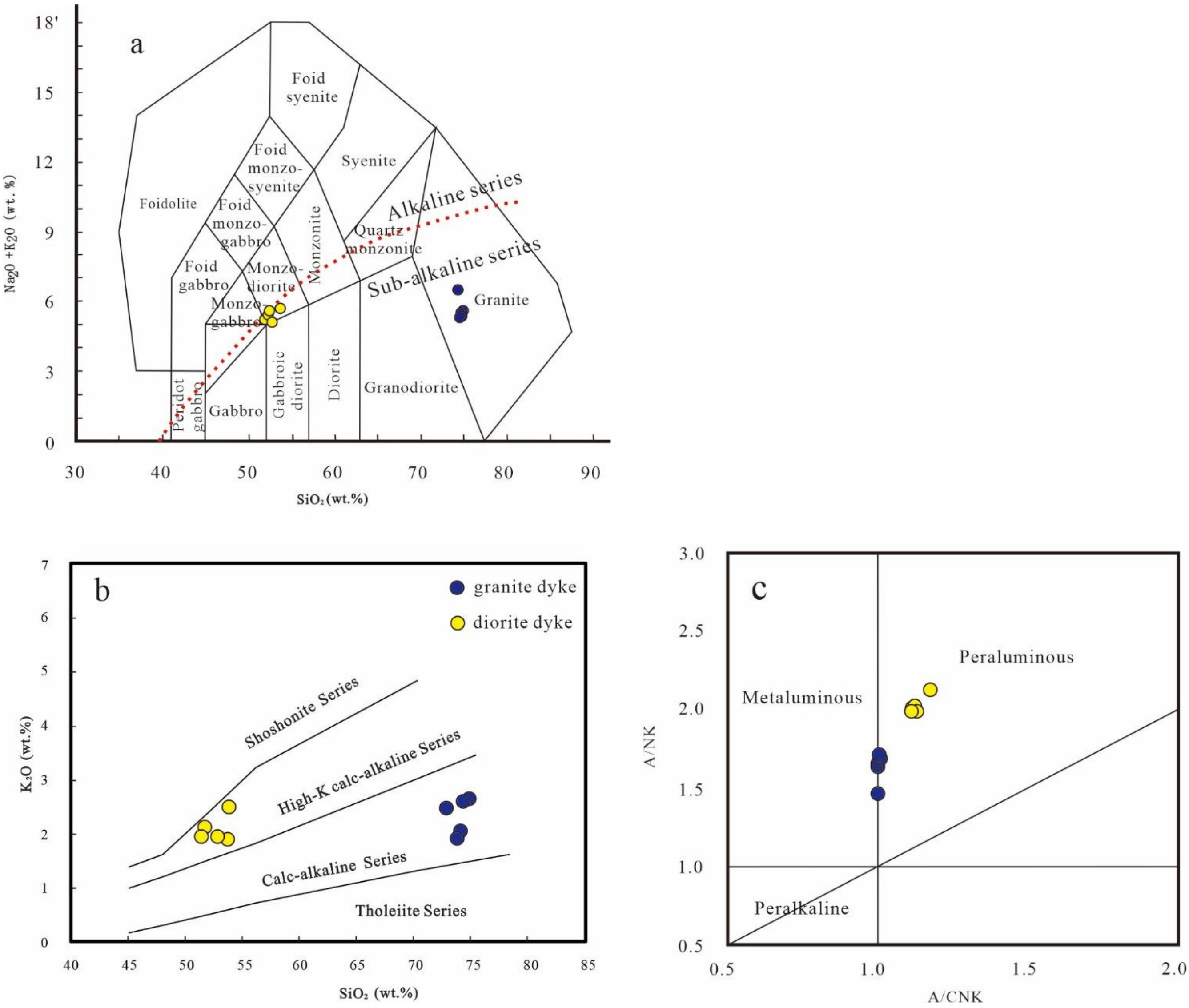

Figure 7. SiO_2–(Na_2O + K_2O), SiO_2–K_2O diagrams and A/NK versus A/CNK. Diagram of the granite and diorite dyke samples. (**a**) Diagram of SiO_2–(Na_2O + K_2O); (base map after Middlemost, [40]). (**b**) Diagram of SiO_2–K_2O (after Peccerillo and Taylor [41]). (**c**) Diagram of A/NK − A/CNK (after Maniar and Piccoli [42]).

In the TAS diagram, all granite data points fall into the granite range, and diorite dykes fall within the monzonite range. In the K_2O vs. SiO_2 diagram, granite plots in the calc-alkaline series (Figure 7b), and diorite dykes plots in the high-K, calc-alkaline series. In the A/CNK vs. A/NK diagram (Figure 7c), granite dykes are located at the junction of the metaluminous and peraluminous fields, and diorite dykes fall within the hyperaluminous range.

4.3.2. Trace Elements

The total rare earth element content of the granite dykes is 93.80~99.63 μg/g. The standardized chondrite rare earth element diagram (Figure 8a) shows that LREE elements are evidently enriched, and the ratios of $(La/Yb)_N$ and La/Yb are 5.44–7.31 and 7.58–10.20, respectively. There is a clear Eu anomaly (Eu/Eu* = 0.62–0.66, average 0.64), and Yb content is 2.03~2.56 μg/g, with an average of 2.26 μg/g. The normalized trace element distribution diagram of the original mantle (Figure 8b) shows that diabase is enriched in LILE (Rb, K, and Sr) and depleted in HFSE (Nb, Ta, Zr, Hf, and Ti).

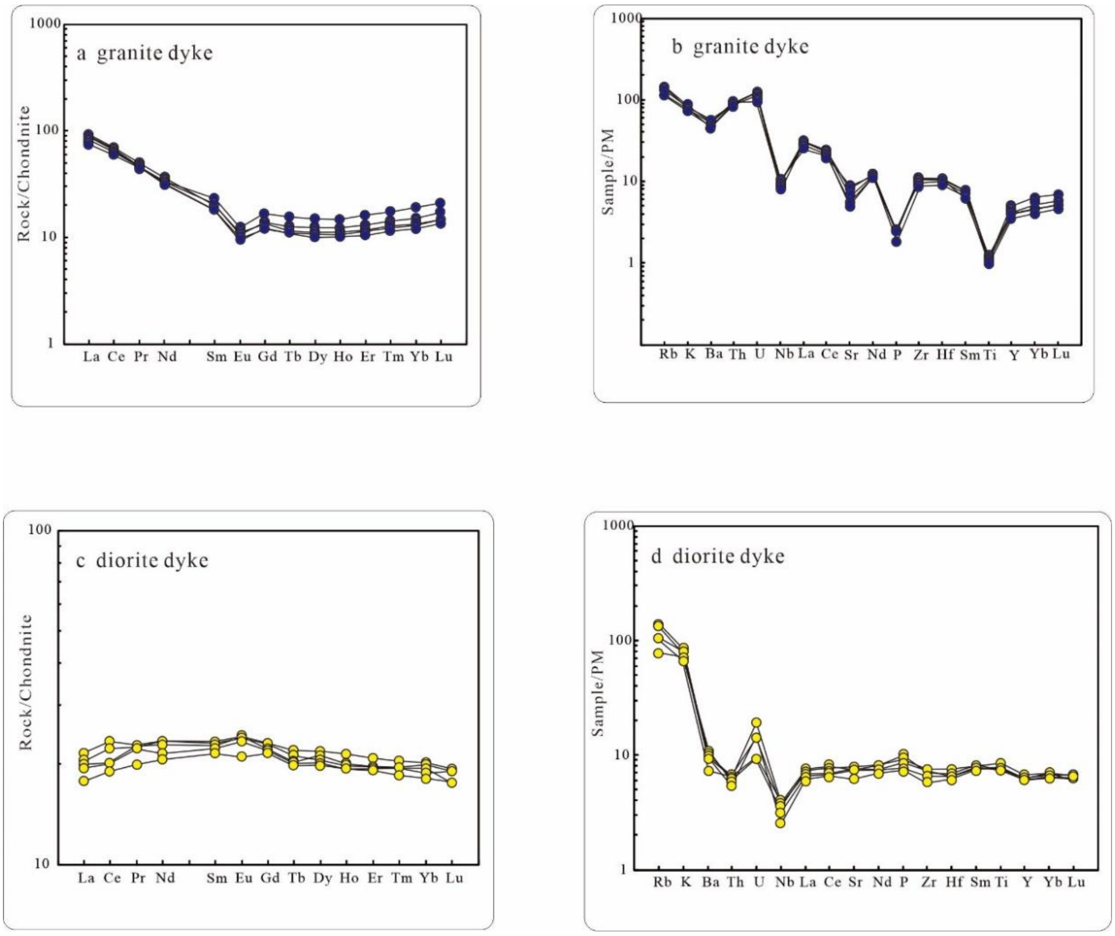

Figure 8. Plots of chondrite-normalized REE patterns and plots of primitive mantle-normalized trace element patterns for the granite and diorite dykes in the Jinba deposit (primitive mantle-normalized values and chondrite-normalized values are from Boynton [43] (1984) and Sun et al. [44] (1989)).

The total rare earth content of diorite dykes is 50.36~56.52 μg/g. The chondrite normalized REE diagram (Figure 8c) shows obvious enrichment of LREE, with $(La/Yb)_N$ and La/Yb ratios ranging from 0.98 to 1.15 and 1.37 to 1.61. The Eu anomalies of all samples are not obvious (Eu/Eu* = 0.93–1.1 average 1.04). The Yb content was low in 3.07~3.41 μg/g, with an average of 3.27 μg/g. In the original mantle-normalized trace element distribution curve (Figure 8d), samples show enrichment of LILEs (Rb, Th, Ba, K) and depletion of HFSEs (Ta, Nb, Ti).

5. Discussion

5.1. Emplacement Ages of Dykes and Magmatism

Plagioclase granite dykes (Habahe pluton) are important orebody host rocks of the Jinba gold deposit. This pluton is widely exposed in the region and crops out over an area of 540 km^2. Researchers have conducted a large number of chronological studies on the Habahe pluton and suggested the emplacement ages of the pluton are within the range of 406 to 390 Ma [23,45]. The age of mafic dykes from the Habahe pluton is 375 Ma [46]. Zircon U–Pb ages of granite and diorite dykes intruding the Habahe pluton are 384.5 ± 1.2 Ma (MSWD = 0.42, n = 29) and 393.0 ± 2.2 Ma (MSWD = 0.10, n = 12), respectively. Extensive alteration and mineralization are observed on the edges and/or inner parts of some diorite dykes, indicating a close relationship with gold mineralization.

There is no accurate mineralization age data for the Jinba gold deposit to date, while a lot of chronological data (Table 4) have been reported for the Zhelande and Saidu gold deposits, located ~15 km and ~10 km northwest of the Jinba deposit, respectively. These three deposits are all emplaced in Devonian strata and within the Markakuli shear zone, which is controlled by NW-trending faults. They all have similar mineralization types (quartz-vein + altered-rock types), mineral assemblages, fluid characters, and isotope composition [47–49], suggesting the same geodynamic setting and metallogenic timing. The interpreted age of gold mineralization is based on Rb–Sr, K–Ar, and Ar–Ar ages of alteration minerals and FIs in ore-bearing quartz veins [19,23,45,50–54]. Mineralization in the region is interpreted to have occurred between ca. 300 and 270 Ma with a peak value of ~290 Ma, which is consistent with the period of orogenic events in the region during the Late Carboniferous–Early Permian.

Table 4. Isotopic ages of rocks and minerals from the Jinba gold deposit.

Test Object	Location	Method	Age	Reference
Plagioclase granite	Jinba	U–Pb	406 Ma	[23]
Plagioclase granite	Jinba	SHRIMP U–Pb	390 ± 5 Ma	[45]
Diorite	Jinba	U–Pb	393.0 ± 2.2 Ma	This study
Granite	Jinba	U–Pb	384.5 ± 1.2 Ma	This study [50]
FIs from ore-bearing quartz vein hosted in Devonian strata	Saidu	Rb-Sr	294~306 Ma	[50]
FIs from ore-bearing quartz vein hosted in Habahe pluton	Saidu	Rb-Sr	272 ± 19 Ma	[51]
Sericite from ore-bearing quartz vein	Saidu	^{40}Ar/^{39}Ar	289.2 ± 3.1 Ma	[52]
Muscovite from ore-bearing quartz vein	Saidu	^{40}Ar/^{39}Ar	294.7 ± 3.5 Ma	[53]
Biotite from ore-bearing quartz vein	Saidu	^{40}Ar/^{39}Ar	270 ± 2.5 Ma	[19]
Biotite from ore-bearing phyllites	Zhelande	K-Ar	297.3 ± 3.3 Ma	[19]
Muscovite from ore-bearing quartz vein	Zhelande	K-Ar	293.4 ± 3.1 Ma	[19]
FIs from ore-bearing quartz vein	Zhelande	Rb-Sr	306.1 ± 5.0 Ma	[19]
Muscovite from ore-bearing quartz vein	Zhelande	^{40}Ar/^{39}Ar	295.4 ± 1.6 Ma	[54]

It can be seen from the above research that the ore-forming age and the dyke emplacement age of the Jinba gold deposit are not consistent, which indicates that there is no centralized or large-scale mineralization in the initial emplacement of dykes. As an orogenic gold deposit, the minerals of the Jinba gold deposit are mainly derived from diorite and Ashele formation rocks [22], that is to say, diorite dykes provide metal ore-forming materials for mineralization.

5.2. Petrogenesis of the Dykes

5.2.1. Granite Dyke

The granitic dykes are calc-alkaline, weakly peraluminous and have the characteristics of differentiated I-type granites [55]. In addition, the rock does not contain cordierite, garnet, or white mica. The content of P_2O_5 is far less than 0.15%, and the content of $K_2O + Na_2O$ is low. Judging from 10,000 × Ga/Al, the granite dykes are neither S-type nor A-type. It can be seen from Figure 9a,b that the granite dykes are I-type granites. Rb/Sr values in the granitic dykes (0.40–0.88) are significantly higher than the Rb/Sr values in the upper crust (0.25), indicating that the rocks have undergone separation crystallization. As can be seen from Figure 9c, the granitic dykes have also undergone differentiation. Thus, the granite dykes belong to I-type granites which are formed by crystallization differentiation.

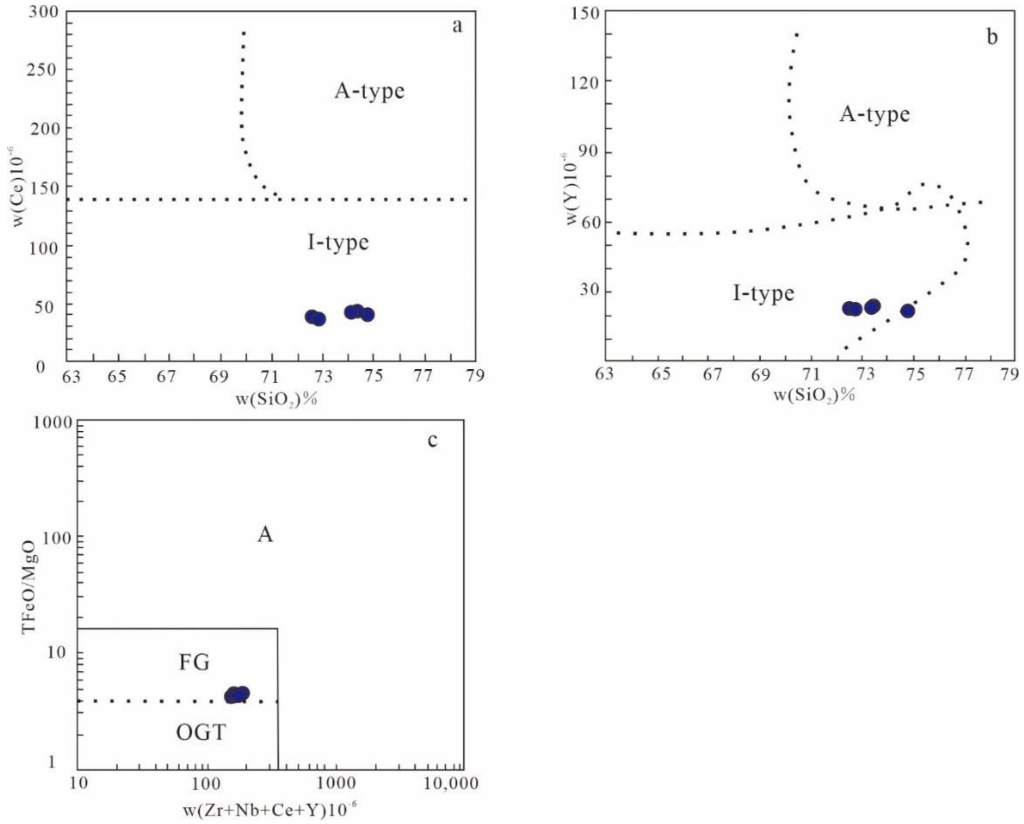

Figure 9. Genetic discrimination map of granitic dykes. (**a**) Ce and SiO_2 granite dykes discriminant diagrams (Collins et al. [56]); (**b**) Y and SiO_2 granites dykes discriminant diagram (Collins et al. [56]); (**c**) T FeO/MgO and Zr + Nb + Ce + Y granites (Whalen, [57]). FG—fractionation acid granites; OGT—unfractionation M, I, and S type granites.

Moreover, the high $\varepsilon_{Hf}(t)$ and the relatively young T_{DM} of the depleted mantle model suggest that the granitic dykes may have originated from a relatively young source region, possibly through fractional crystallization or early partial melting of mantle-derived magma. The linear relationship between the ratio of K/Rb and K/Cs and SiO_2 is not very obvious, suggesting that the fractional crystallization of magma is not strong. At the same time, the relationship between La/Sm and La showed a significant positive correlation, indicating that although a certain degree of crystallization differentiation occurred during the ascending emplacement of magma, it was mainly controlled by partial melting. The Nb/Ta values of all samples range from 11.6 to 13.4, and the Zr/Hf values range from 34.1 to 35.2, which are close to the corresponding crustal element ratios of 11 and 33, respectively. The Th/Ta ratios of the samples range from 12.6 to 14.9, which is comparable to the Th/Ta ratios of the crust (approximately 10) [58]. The samples have low Sr contents (102.5–188 μg/g), Al_2O_3 (12.9%–14.0%), and Ti/Zr of less than 20 (11.8–14.4), which indicates that the granitic veins are typical partial melting products of the continental crust [59,60]. All the rocks have an obvious negative Eu anomaly, with a strong depletion in Sr, P, Ti, and other elements, Zr/Sm > 10 (32.9–43.6), and high Yb content (2.03–2.56 μg/g), indicating that there are plagioclase, apatite, and hornblende residues in the mineral facies of the asthenosphere [61]. Therefore, it is considered that the granite dykes are mainly formed by mixing and melting of crustal and mantle materials with slight crystallization differentiation.

5.2.2. Diorite Dykes

The main elements are positively correlated with the change of MgO content, indicating that there may be some separated crystallization in the process of magmatism. Cr and Ni contents in diorite dykes are low (10–20 μg/g and 4.8–6.7 μg/g), and lower than those of primary basaltic magma (300–400 μg/g and 300–500 μg/g) [62]. This indicates that the diorite dyke magma experienced significant separation crystallization of mafic minerals such as olivine, monoclinic pyroxene, and ferrotitanium oxides. The diorite dykes are depleted of rare earth elements in different degrees and the chondrite normalized REE distribution curve, and all samples have the same variation trend and typical N-MORB REE geochemical characteristics, indicating that the diorite dykes derived from the depleted asthenospheric mantle. All the samples are characterized by an enrichment of large ion lithophile elements (Rb, Th, Ba, K) and depletion of high field strength elements (Ta, Nb, Ti), indicating that the magma source was contaminated and metasomatized by crustal components [63]. Ti/Zr values range from 11.2 to 18.1, and Ti/Y values range from 31.5 to 41.3, which is close to crustal contents (Ti/Zr < 30, Ti/Y < 200) [64,65]. Rb/Sr values range from 0.31 to 0.64, indicating a crustal origin [66]; thus, the original magma was mixed with crustal materials to a certain extent during magma ascension. In addition, the Lu–Hf isotopic system in zircon can explain magma origin and petrogenesis [67,68]. Indeed, $\varepsilon_{Hf(t)}$ values of diorite dykes range from −1.18 to −4.47, and T_{DM2} values range from 1242 to 1668 Ma, indicating that the magma may have both relatively ancient lower crust and depleted mantle components. In addition, the high Nb and Ta contents (1.8–2.8 ppm, 0.11–0.16 ppm) also indicate the obvious crustal mixing. The mixing of depleted mantle and ancient crust led to a change in $\varepsilon_{Hf(t)}$, and the degree of change depends on the mixing ratio of the two [69]. Thus, in general, the diorite dykes were the product of rising mantle magma that underwent mafic mineral crystallization and mixing with crustal material.

5.3. Tectonic Setting

The granite dykes have obvious characteristics of I-type granites and high Th/Ta ratio (12.6–14.9), which are geochemical characteristics of subduction zone magma. In addition, the granitic dykes have low Yb, Ta, and Th contents, enrichment of U, Pb, and LREE, depletion of Ti, P, Sr, and Ba, negative Nb and Ta anomalies, and weak negative Eu anomalies, similar to island arc magmatic rocks in subduction zones. In the Nb-Y and Rb-Y + Nb discrimination diagrams for granitic dykes (Figure 10), all samples fall within the volcanic arc granite region. The granitic dykes are depleted of P, Nb, Ti, Sr and enriched in Rb, Th, K, La, and the Hf isotope indicates that the granitic dykes have an obvious addition of continental crust material, indicating that the granitic dykes were formed in an island arc environment on active continental margins.

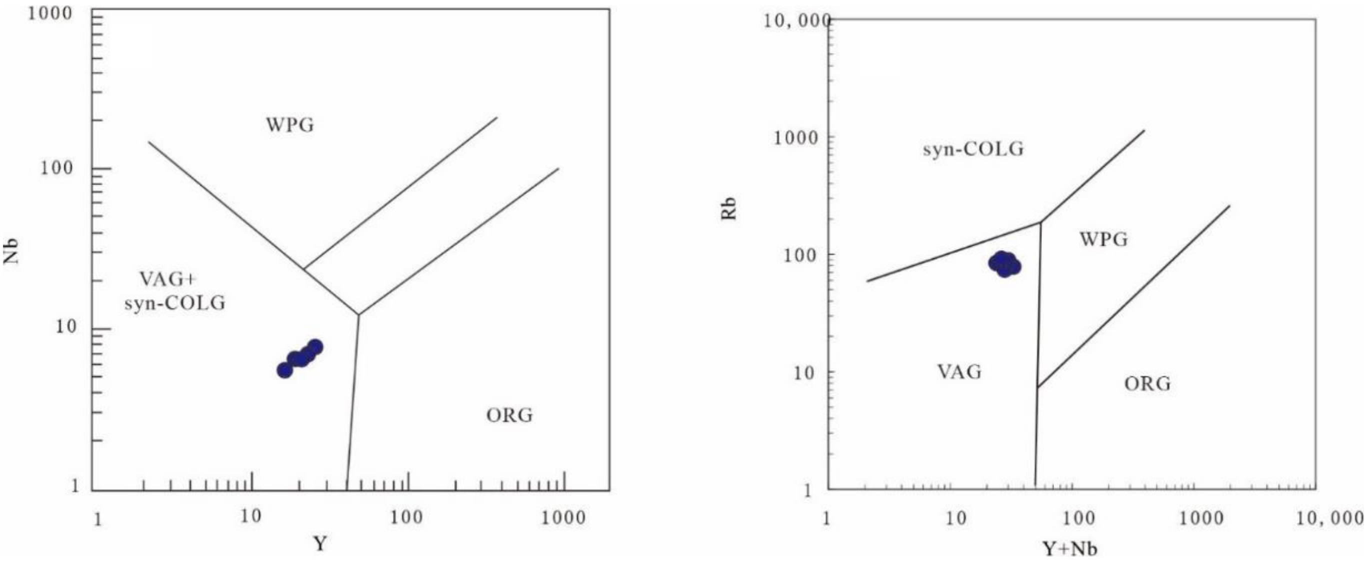

Figure 10. Discriminant diagram of granite dyke tectonic environment in the Jinba deposit (according to Pearce et al. [70]). WPG—intraplate granite; VAG—volcanic arc granite; Syn-COLG—syn-collisional granite; ORG—ocean ridge granite.

Diorite dykes show similar compositions to N-MORB in Nb/Yb-Th/Yb (Figure 11a), which point towards mantle sources. In addition, the Nb and Ta contents of diorite dykes are 1.8–2.8 μg/g and 0.11–0.16 μg/g, respectively, which are similar to typical island arc tholeiite (1.7–2.7 μg/g, 0.1–0.18 μg/g). In V-Ti/1000 (Figure 11b), the samples all fell into the island arc tholeiite area. In general, diorite dykes are enriched in large ion lithophile elements and light rare earth elements and depleted in high field strength elements. Diorite dykes have exactly the same characteristics as subduction-related island arc magmatism [70], so diorite dykes are characterized by continental or island arc magmatism associated with subduction zones [71].

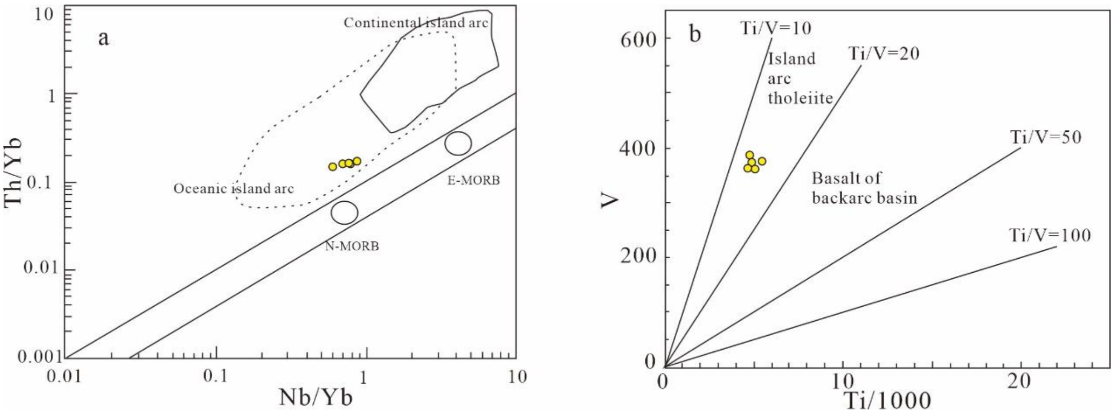

Figure 11. Diorite dyke structure discrimination diagram. (**a**) Nb/Yb-Th/Yb diagram (after Xu et al. [72]); (**b**) Ti-V diagram (after Shervais [73]).

Zircon U–Pb ages of granitic and diorite dykes in the Jinba gold deposit are 384 Ma and 393 Ma, respectively, which belong to the products of Early–Mid-Devonian magmatic activity in the southern margin of the Altay belt. Previous studies have proved that the southern margin of Altay was in an active continental margin environment at this time [14,74–78]. Thus, based on this study, the granitic and diorite dykes of the Jinba gold deposit were formed in an island arc environment related to subduction.

6. Conclusions

1. Zircon U–Pb ages of granite and diorite dykes are 384~393 Ma, indicating Early–Middle Devonian magmatic activity. The mineralization age of Jinba gold deposit is Late Carboniferous–Early Permian. The mineralization age of the Jinba gold deposit does not coincide with granite dykes and diorite dykes.
2. The granite dykes are mainly formed by the mixing and melting of crustal and mantle materials with slight crystallization differentiation, while diorite dykes are the product of rising mantle magma that underwent crystallization of mafic minerals and mixing with crustal material.
3. The granitic and diorite dykes of the Jinba gold deposit were formed in an island arc environment related to subduction.

Author Contributions: Conceptualization: F.X.; methodology: S.L.; software and validation: L.G.; formal analysis and investigation: C.C.; resources: C.C.; data curation: F.X.; writing—original draft preparation: F.X.; writing—review and editing: F.X.; visualization: F.X.; supervision: F.X.; project administration: S.L.; funding acquisition: S.L. All authors have read and agreed to the published version of the manuscript.

Funding: This work was supported by the Natural Science Foundation of the Xinjiang Uygur Autonomous Region (2020D01C075).

Acknowledgments: We give thanks to the Xinjiang Jinba gold mine staff for their assistance in field work. Thanks to the chief editor and reviewers for their review and constructive comments, which have played a great role in the improvement of this paper.

Conflicts of Interest: The authors declare no conflict of interest.

References

1. Sengör, A.M.C.; Natalin, B.A.; Burtman, V.S. Evolution of the Altaid tectonic collage and Palaeozoic crustal growth in Eurasia. *Nature* **1993**, *364*, 299–307. [CrossRef]
2. Xiao, W.J.; Kröner, A.; Windley, B.F. Geodynamic evolution of Central Asia in the Paleozoic and Mesozoic. *Int. J. Earth Sci.* **2009**, *98*, 1185–1188. [CrossRef]
3. Xiao, W.; Huang, B.; Han, C.; Sun, S.; Li, J. A review of the western part of the Altaids: A key to understanding the architecture of accretionary orogens. *Gondwana Res.* **2010**, *18*, 253–273. [CrossRef]
4. Safonova, I.Y.; Santosh, M. Accretionary complexes in the Asia-Pacific region: Tracing archives of ocean plate stratigraphy and tracking mantle plumes. *Gondwana Res.* **2014**, *25*, 126–158. [CrossRef]
5. Kröner, A.; Kovach, V.; Belousova, E.; Hegner, E.; Armstrong, R.; Dolgopolova, A.; Seltmann, R.; Alexeiev, D.V.; Hoffmann, J.E.; Wong, J.; et al. Reassessment of continental growth during the accretionary history of the Central Asian Orogenic Belt. *Gondwana Res.* **2014**, *25*, 103–125. [CrossRef]
6. Yakubchuk, A. Evolution of the Central Asian Orogenic Supercollage since Late Neoproterozoic revised again. *Gondwana Res.* **2017**, *47*, 372–398. [CrossRef]
7. Xiao, X.C.; Tang, Y.Q.; Feng, Y.M.; Zhu, B.Q.; Li, J.Y.; Zhao, M. *Tectonic Evolution of Northern Xinjiang and Its Adjacent Regions*; Geological Publishing House: Beijing, China, 1992; pp. 1–169, (In Chinese with English Abstract)
8. He, G.Q.; Li, M.S.; Li, D.Q.; Zhou, N.H. *Paleozoic Crustal Evolution and Minerlization in Xinjiang, China*; Xinjiang People's Publishing House: Urumqi, China, 1994; pp. 1–437. (In Chinese)
9. Windley, B.F.; Alexeiev, D.; Xiao, W.J.; Kröner, A.; Badarch, G. Tectonic models for accretion of the Central Asian Orogenic Belt. *J. Geol. Soc.* **2007**, *164*, 31–47. [CrossRef]
10. Xiao, W.; Sun, M.; Santosh, M. Continental reconstruction and metallogeny of the Circum-Junggar areas and termination of the southern Central Asian Orogenic Belt. *Geosci. Front.* **2015**, *6*, 137–140. [CrossRef]
11. Zhao, Z.H.; Wang, Z.G.; Zou, T.R.; Masuda, A.; Tu, G.Z. The REE, isotopic composition of O, Pb, Sr and Nd and petrogenesis of granitoids in the Altai region. In *Progress of Solid-Earth Sciences in Northern Xinjiang, China*; Tu, G.C., Ed.; Science Press: Beijing, China, 1993; pp. 239–266. (In Chinese with English Abstract)
12. Wang, Z.G.; Zhao, Z.H.; Zou, T.R. *Geochemistry of the Granitoids in Altay*; Science Press: Beijing, China, 1998; pp. 1–152. (In Chinese with English Abstract)
13. Wang, T.; Hong, D.W.; Tong, Y.; Han, B.-F. Zircon U-Pb SHRIM Page and origin of post-orogenic Lamazhao granitic pluton from Altai orogen: Its implications for continental growth. *Acta Petrol. Sin.* **2005**, *21*, 640–650. (In Chinese with English Abstract)
14. Tong, Y.; Wang, T.; Hong, D.W.; Dai, Y.J. Ages and origin of the early Devonian granites from the north part of Chinese Altai M ountains and its tectonic implications. *Acta Petrol. Sin.* **2007**, *23*, 1933–1944. (In Chinese with English Abstract)
15. Chai, F.M.; Ouyang, L.J.; Dong, L.H.; Yang, F.Q.; Liu, F.; Zhang, Z.X.; Li, Q. Geochronology and geochemistry of tonodiorite in The Ashele Copper-Zinc Deposit, Xinjiang. *Chin. J. Petrol. Mineral.* **2013**, *32*, 41–52. (In Chinese with English Abstract)
16. Gao, L.-L.; Chen, C.; Wang, K.-Y.; Zhang, X.-B.; Li, S.-D. Tectonic setting and geochronology of the Sarsuk Au polymetallic deposit in Xinjiang, NW China: Constraints from pyrite Re–Os, zircon U–Pb dating and Hf isotopes. *Ore Geol. Rev.* **2020**, *124*, 103641. [CrossRef]
17. Xiao, W.J.; Pirajno, F.; Seltmann, R.; Safonova, I.; Chen, Y.J.; Muhtar, M.N. Metallogeny of the Southern Altaids: Key to Understanding the Accretionary Tectonics and Crustal Evolution of Central Asia. *Ore Geol. Rev.* **2022**, *144*, 104871. [CrossRef]
18. Chen, K.Q.; Dang, Y.X.; Dong, Y.G.; Ding, R.F. Zircon U–Pb age of the Au–bearing quartz veins in Saidu gold deposit and its geological implications. *Miner. Explor.* **2010**, *1*, 229–233. (In Chinese with English Abstract)
19. Deng, S.L. Mineralation of Ductile Shear Belt Gold Deposit of Maerkakuli in Habahe, Xinjiang. Master's Thesis, Chengdu University of Technology, Chengdu, China, 2011. (In Chinese with English Abstract)
20. Zhan, S.; Tian, Z.F.; Song, M.Y. Stable isotope characteristics of typical deposits in Habahe Gold belt, Xinjiang. *Xinjiang Geol.* **2016**, *34*, 476–480. (In Chinese with English Abstract)
21. Wang, Y.W.; Xu, J.H.; Wei, X.F.; Ding, R.F. The mineralization of the Jinba gold deposit, Xinjiang, China: Evidence from Geology and Fluid inclusions. *Earth Sci.* **2018**, *43*, 14.
22. Li, S.-D.; Chen, C.; Gao, L.-L.; Xia, F.; Zhang, X.-B.; Wang, K.-Y. Fluid Inclusions and H–O–C–S–Pb Isotopic Systematics of the Jinba Gold Deposit, NW China: Implications for Ore Genesis. *Front. Earth Sci.* **2021**, *9*, 638375. [CrossRef]
23. Li, Y.; Zhou, G.; Chai, F.M. LA-ICP-MS U-Pb ages and geological implications of the Habahe Pluton at the Southern Margin of the Altay, Xinjiang. *Xinjiang Geol.* **2012**, *30*, 146–151. (In Chinese with English Abstract)
24. Zhang, M.; Niu, X.L.; Mo, L.C.; Niu, S.D.; Wu, H.Y.; Zhou, Q.F. Fluid inclusions characteristics and ore-forming fluid evolution of in the Tuokuzibayi gold deposit in the southern margin of Altay. *Acta Petrol. Sin.* **2020**, *36*, 1171–1185.

25. Pirajno, F.; Seltmann, R.; Yang, Y. A review of mineral systems and associated tectonic settings of northern Xinjiang, NW China. *Geosci. Front.* **2011**, *2*, 47–75. [CrossRef]
26. Tian, X.Y.; Xiao, G.L. Geological characteristics and genesis of Tukuzibayi Gold Deposit in Habahe County, Xinjiang. *Xinjiang Geol.* **2007**, *25*, 258–262. (In Chinese with English Abstract)
27. Chen, H.Y.; Chen, Y.J.; Liu, Y.L. Mineralization of Erqis gold belt in Xinjiang and its relation to Central Asian Orogenesis. *Sci. China Ser. D* **2000**, *30*, 38–44.
28. Liu, Y.S.; Hu, Z.C.; Gao, S.; Gunther, D.; Xu, J.; Gao, C.G.; Chen, H.H. In situ analysis of major and trace elements of anhydrous minerals by LA-ICP-MS without applying an internal standard. *Chem. Geol.* **2008**, *257*, 34–43. (In Chinese with English Abstract) [CrossRef]
29. Wiedenbeck, M.; Alle, P.; Corfu, F.; Griffin, W.L.; Meier, M.; Oberli, F.; Vonquadt, A.; Roddick, J.C.; Speigel, W. Three natural zircon standards for U-Th-Pb, Lu-Hf, trace-element and REE analyses. *Geostand. Newsl.* **1995**, *19*, 1–23. [CrossRef]
30. Ludwig, K.R. *ISOPLOT 3.0: A Geochronological Toolkit for Microsoft Excel*; Berkeley Geochronology Center Special Publication: Berkeley, CA, USA, 2003; pp. 1–70.
31. Chen, Q.Z.; Jiang, S.Y.; Duan, R.C. The geochemistry, U-Pb and Re-Os geochronology, and Hf isotopic constraints on the genesis of the Huangjiagou Mo deposit and related granite in the Dabie region, Hubei Province, China. *Ore Geol. Rev.* **2017**, *81*, 504–517. [CrossRef]
32. Griffin, W.L.; Pearson, N.J.; Belousova, E.; Jackson, S.; van Achterbergh, E.; O'Reilly, S.Y.; Shee, S. The Hf isotope composition of cratonic mantle: LAM-MC-ICPMS analysis of zircon megacrysts in kimberlites. *Geochim. Cosmochim. Acta* **2000**, *64*, 133–147. [CrossRef]
33. Geng, J.Z.; Li, H.K.; Zhang, J.; Zhou, H.Y.; Li, H.M. Zircon Hf isotope analysis by means of LA-MC-ICP-MS. *Geol. Bull. China* **2011**, *30*, 1508–1513. (In Chinese with English Abstract)
34. Griffin, W.L.; Wang, X.; Jackson, S.E.; Pearson, N.J.; O'Reilly, S.Y.; Xu, X.; Zhou, X. Zircon chemistry and magma mixing, SE China; in-situ analysis of Hf isotopes, Tonglu and Pingtan igneous complexes. *Lithos* **2002**, *61*, 237–269. [CrossRef]
35. Peytcheva, I.; Quadt, A.V.; Neubauer, F.; Frank, M.; Nedialkov, R.; Heinrich, C.; Strashimirov, S. U-Pb dating, Hf-isotope characteristics and trace-REE-patterns of zircons from Medet porphyry copper deposit, Bulgaria: Implications for timing, duration and sources of ore-bearing magmatism. *Mineral. Petrol.* **2009**, *96*, 19–41. [CrossRef]
36. Scherer, E.E.; Cameron, K.L.; Blichert-Toft, J. Lu-Hf garnet geochronology: Closure temperature relative to the Sm-Nd system and the effects of trace mineral inclusions. *Geochim. Cosmochim. Acta* **2000**, *64*, 3413–3432. [CrossRef]
37. Hoskin, P.W.O.; Black, L.P. Metamorphic zircon formation by solid-state recrystallization of protolith igneous zircon. *J. Metamorph. Geol.* **2000**, *18*, 423–439. [CrossRef]
38. Soderlund, U.; Patchett, P.; Vervoort, J.D.; Isachsen, C.E. The176Lu decay constant determined by Lu-Hf andU-Pb isotope systematics of Precambrian mafic intrusions. *Earth Planet. Sci. Lett.* **2004**, *219*, 311–324. [CrossRef]
39. Guo, C.L.; Chen, Y.C.; Zeng, Z.L.; Lou, F. Petrogenesis of the Xihuashan granites in southeastern China: Constraints from geochemistry and in-situ analyses of zircon U-Pb-Hf-O isotopes. *Lithos* **2012**, *148*, 209–227. [CrossRef]
40. Middlemost, E.A.K. Naming materials in the magma/igneous rock system. *Earth Sci. Rev.* **1994**, *37*, 215–224. [CrossRef]
41. Peccerillo, A.; Taylor, S.R. Geochemistry of Eocene calc-alkaline volcanic rocks from the Kastamonu area, northern Turkey. *Contrib. Mineral. Petrol.* **1976**, *58*, 63–81. [CrossRef]
42. Maniar, P.D.; Piccoli, P.M. Tectonic discrimination of granitoids. *Geol. Soc. Am. Bull.* **1989**, *101*, 635–643. [CrossRef]
43. Boynton, W.V. Geochemistry of the Rare Earth Elements: Meteorite Studies. In *Rare Earth Element Geochemistry*; Henderson, P., Ed.; Elsevier: Amsterdam, The Netherlands, 1984; pp. 63–114.
44. Sun, S.S.; McDonough, W.F. *Chemical and Isotopic Systematics of Oceanic Basalts: Implications for Mantle Composition and Processes*; Geological Society, London, Special Publications: London, UK, 1989; Volume 42, pp. 313–345.
45. Cai, K.D. Magmatism of the Western Chinese Altai Orogen: Geochronology, Petrogenesis and Tectonic Implications. Master's Thesis, Chinese Academy of Sciences, Beijing, China, 2007. (In Chinese with English Abstract)
46. Cai, K.; Sun, M.; Yuan, C.; Zhao, G.; Xiao, W.; Long, X.; Wu, F. Geochronological and geochemical study of mafic dykes from the northwest Chinese Altai: Implications for petrogenesis and tectonic evolution. *Gondwana Res.* **2010**, *18*, 638–652. [CrossRef]
47. Xu, J.H.; Zhang, G.R.; Xie, Y.L.; Shan, L.H.; Zhang, S.J.; Wang, P.H.; Zou, C.H. The evolution of teconic-metallogenic fluids in the Saidu gold deposit, Southern Altay. *Acta Petrol. Mineral.* **2009**, *28*, 141–151. (In Chinese with English Abstract)
48. Mi, D.J.; Su, D.Y.; Zou, C.H.; Tang, X.D. Geological characteristics of Saidu gold deposit in Habahe County of Xinjiang autonomous region. *Contrib. Geol. Miner. Resour. Res.* **2010**, *25*, 331–335. (In Chinese with English Abstract)
49. Xue, X.L. Geological characteristics and geneses of Zanlander gold deposit, Habahe County, Xinjiang. *World Nonferrous Metal.* **2018**, *4*, 150. (In Chinese with English Abstract)
50. Li, H.Q.; Chen, F.W. *Chronology of Regional Mineralization in Xinjiang, China*; Geological Publishing House: Beijing, China, 2004; pp. 40–45. (In Chinese with English Abstract)
51. Yan, S.H.; Teng, R.L.; Wang, Y.T.; Chen, W.; Chen, B.L. 40Ar/39Ar dating of the Bu'ergen gold-bearing shear zone on the southern margin of the Altay Mountains, Xinjiang, and its significance. *Geol. China* **2006**, *33*, 648–655. (In Chinese with English Abstract)
52. Rui, X.; Zhu, S. The main characteristics and regional metallogenic model of Altay primary gold deposits in Xinjiang. *Geol. Rev.* **1994**, *39*, 138–148. (In Chinese with English Abstract)

53. Li, G.M.; Shen, Y.C.; Liu, T.B.; Shen, P.; Zhou, N.W. Metallogenic evolution of Tuokuzibayi gold deposit in southern Altay, north Xinjiang:Evidence from characteristics of quartz vein systems, isotopic geochemistry and Ar-Ar chronology. *Miner. Depos.* **2007**, *1*, 15–32, (In Chinese with English Abstract)
54. Liu, G.-R.; Li, Y.; Wang, R.; Wang, H.-P.; Yang, C.-D.; Chen, Q.; Qi, S.-J. ^{40}Ar/^{39}Ar dating of Muscovite from the Zhelande Au deposit, Irtysh tectonic zone, Xinjiang and Its Geological Implications. *Rock Miner. Anal.* **2018**, *37*, 705–712.
55. Chappell, B.W. Aluminium saturation in I- and S-type granites and the characterization of fractionated haplogranite. *Lithos* **2000**, *46*, 535–551. [CrossRef]
56. Collins, W.J.; Beams, S.D.; White, A.J.R.; Chappell, B.W. Nature and origin of A-type granites with particular reference to southeastern Australia. *Contrib. Mineral. Petrol.* **1982**, *80*, 189–200. [CrossRef]
57. Whalen, J.B.; Currie, K.L.; Chappell, B.W. A-type granites: Geochemical characteristics, discrimination and petrogenesis. *Contrib. Mineral. Petrol.* **1987**, *95*, 407–419. [CrossRef]
58. McDonough, W.F.; Sun, S.S. The composition of the earth. *Chem. Geol.* **1995**, *120*, 223–253. [CrossRef]
59. Wilson, M. *Igneous Petrogenesis*; Unwin Hyman Press: London, UK, 1989; pp. 295–323.
60. Francalanci, L.; Taylorsr, S.R.; Mcculloch, M.T. Geochemical and isotopic variations in the calcalkaline rocks of Aeolian arc, southern Tyrrhenian Sea, Italy: Constraints on magma genesis. *Contrib. Mineral. Petrol.* **1993**, *113*, 300–313. [CrossRef]
61. Lightfoot, P.C.; Hawkesworth, C.J.; Sethna, S.F. Petrogenesis of rhyolites and trachytes from the Deccan trap: Sr, N and Pb isotope and t race element evidence. *Contrib. Mineral. Petrol.* **1987**, *95*, 44–54. [CrossRef]
62. Frey, F.A.; Gerlach, D.C.; Hickey, R.L.; Lopez-Escobar, L.; Munizaga-Villavicencio, F. Petrogenesis of the Laguna del Maule volcanic complex, Chile (36° S). *Contrib. Mineral. Petrol.* **1984**, *88*, 133–149. [CrossRef]
63. Ryerson, F.J.; Watson, E.B. Rutile Saturation in Magmas: Implications for Ti-Nb-Ta Depletion in Island-Arc Basalts. *Earth Planet. Sci. Lett.* **1987**, *86*, 225–239. [CrossRef]
64. Jagoutz, O.; Schmidt, M.W. The composition of the foundered complement to the continental crust and a re-evaluation of fluxes in arcs. *Earth Planet. Sci. Lett.* **2013**, *371–372*, 177–190. [CrossRef]
65. Wedepohl, K.H. The Composition of the Continental Crust. *Geochim. Cosmochim. Acta* **1995**, *59*, 1217–1232. [CrossRef]
66. Taylor, S.R.; Mclennan, S.M. The geochemical evolution of the continental crust. *Rev. Geophys.* **1995**, *33*, 241–265. [CrossRef]
67. Kemp, A.; Hawkesworth, C.J.; Paterson, B.A.; Kinny, P.D. Episodic growth of the Gondwana supercontinent from hafnium and oxygen isotopes in zircon. *Nature* **2006**, *439*, 580–583. [CrossRef]
68. Yang, J.-H.; Wu, F.-Y.; Wilde, S.A.; Xie, L.-W.; Yang, Y.-H.; Liu, X.-M. Tracing magma mixing in granite genesis: In situ U–Pb dating and Hf-isotope analysis of zircons. *Contrib. Mineral. Petrol.* **2007**, *153*, 177–190. [CrossRef]
69. Ji, W.Q.; Wu, F.Y.; Chung, S.L.; Li, J.X.; Liu, C.Z. Zircon U–Pb geochronology and Hf isotopic constraints on petrogenesis of the Gangdese batholith, southern Tibet. *Chem. Geol.* **2009**, *262*, 229–245. [CrossRef]
70. Pearce, J.A.; Peate, D.W. Tectonic Implications of the Composition of Volcanic ARC Magmas. *Annu. Rev. Earth Planet. Sci. Lett.* **1995**, *23*, 251–285. [CrossRef]
71. Kelemen, P.B.; Hanghj, K.; Greene, A.R. One View of the Geochemistry of Subduction-Related Magmatic Arcs, with an Emphasis on Primitive Andesite and Lower Crust. *Treatise Geochem.* **2007**, *3*, 1–70.
72. Xu, J.F.; Castillo, P.R.; Chen, F.R.; Niu, H.C.; Xu, Y.G.; Zhen, Z.P. Geochemistry of late Paleozoic mafic igneous rocks from the Kuerti area, Xinjiang, northwestern China: Implications for back arc mantle evolution. *Chin. Geol.* **2003**, *193*, 137–154. [CrossRef]
73. Shervais, J.W. Ti-V plots and the petrogenesis of modern and ophiolitic lavas. *Earth Planet. Sci. Lett.* **1982**, *59*, 101–118. [CrossRef]
74. Zhang, H.-X.; Niu, H.-C.; Hiroaki, S.; Shan, Q.; Yu, X.-Y.; Ito, J.; Zhang, Q. Late Paleozoic adakite and Nb-enriched basalt from Northern Xinjiang: Evidence for the Southward subduction of the Paleo-Asian Ocean. *Geol. J. China Univ.* **2004**, *10*, 106–113. (In Chinese with English Abstract)
75. Wang, T.; Hong, D.W.; Jahn, B.M.; Tong, Y.; Wang, Y.; Han, B.; Wang, X. Timing, petrogenesis, and setting of Paleozoic synorogenic intrusions from the Altai Mountains, Northwest China: Implications for the tectonic evolution of an accretionary orogen. *J. Geol.* **2006**, *114*, 735–751. [CrossRef]
76. Liu, F.; Yang, F.; Mao, J.; Chai, F.; Geng, X. Study on ch ronology and geochemistry for A bagong g rani te in Altay orogen. *Acta Petrol. Sin.* **2009**, *25*, 1416–1425. (In Chinese with English Abstract)
77. Sun, M.; Long, X.P.; Cai, K.D.; Jiang, Y.; Wang, B.; Yuan, C.; Zhao, G.; Xiao, W.; Wu, F. Early Paleozoic ridge subduction in the Chinese Altai: Insight from the abrupt change in Zircon Hf isotopic compositons. *Sci. China Earth Sci.* **2009**, *39*, 935–948. (In Chinese) [CrossRef]
78. Wang, Y.; Yuan, C.; Long, X.; Sun, M.; Xiao, W. The Kanasi potassic magnesian-rich dacites, Altai, northw estern Chinese: M etasomatism by the melts of subducted sediments. *Chin. J. Geol.* **2010**, *45*, 12–29. (In Chinese with English Abstract)